Modeling the Optical and Radiative Properties of Vertically Aligned Carbon Nanotubes in the Infrared Region

Richard Z. Zhang
George W. Woodruff School of Mechanical Engineering, Georgia Institute of Technology, Atlanta, GA 30332

Xianglei Liu
George W. Woodruff School of Mechanical Engineering, Georgia Institute of Technology, Atlanta, GA 30332

Zhuomin M. Zhang[1]
George W. Woodruff School of Mechanical Engineering, Georgia Institute of Technology, Atlanta, GA 30332
e-mail: zhuomin.zhang@me.gatech.edu

During the past decade, research on carbon nanotubes has revealed potential advances in thermal engineering applications. The present study investigates the radiative absorption and reflection of vertically aligned carbon nanotubes (VACNTs) in the broad spectrum from the near-infrared to far-infrared regions. The optical constants of VACNT are modeled based on the dielectric function of graphite and an effective medium approach that treats the CNT film as a homogenized medium. Calculated radiative properties show characteristics of near-unity index matching and high absorptance up to around 20 μm wavelength. The packing density and degree of alignment are shown to affect the predicted radiative properties. The Brewster angle and penetration depth of VACNTs are examined in the infrared spectrum. The radiative properties for VACNT thin films are also evaluated, showing some reduction of absorptance in the near-infrared due to transmission for film thicknesses less than 50 μm. This study provides a better understanding of the infrared behavior of VACNT and may guide the design for its applications in energy harvesting, space-borne detectors, and stealth technology.
[DOI: 10.1115/1.4030222]

Keywords: carbon nanotubes, effective medium theory, radiative properties, thin film

1 Introduction

It has been demonstrated that aligned CNTs exhibit high absorptance from the visible to infrared wavelength region due to interband transitions and free-electron absorption, as well as impedance matching with air [1]. Because of this, CNT thin films and coatings hold promise in thermal radiation detection and heat transfer applications. For example, they have been used on spacecraft radiometers and bolometers [2,3], pyroelectric radiation detectors and calibrators [4–7], solar microcells [8], and solar thermophotovoltaic devices [9]. Understanding the optical and radiative properties of CNT films in the broad infrared wavelength region is critical for these applications.

The benefit of vertically aligned CNT (VACNT) arrays was noticed two decades ago when similarities between VACNT films and antireflecting glassy carbon were observed through ellipsometry measurements [10]. To obtain the near-unity refractive index to match air or vacuum, single-walled VACNT arrays were grown sparsely packed, resulting in extremely low reflectance in the visible wavelength range [11]. More recent experimental studies also showed ultralow reflectance and near-blackbody emission at the mid-infrared wavelengths from 3 μm to 13 μm [12]. Mizuno et al. [13] reported VACNT absorptance exceeding 0.98 across a wide wavelength range from the ultraviolet (UV) (wavelength $\lambda = 200$ nm) to the far-infrared ($\lambda = 200$ μm) using combined spectroscopic reflectance and emission measurements. Wang et al. [14,15] demonstrated high absorptance of multiwalled VACNTs having either diffuse or specular characteristics. Ye et al. [16] demonstrated that the alignment has a strong effect on the infrared absorption coefficient of VACNT films. While the optical properties of single-walled and double-walled CNTs have been investigated by several groups [17–22], these studies used randomly aligned CNTs and obtained relatively high reflectance in the far-infrared region. Paul et al. [23] used transmission ellipsometry to obtain the ordinary and extraordinary components of the optical constants of multiwalled VACNT films in the limited frequency region from 0.4 THz to 1.6 THz (i.e., 750 μm to 190 μm wavelengths). Their experiment demonstrates the potential of VACNT as highly absorbing coatings in the far-infrared. Therefore, it is important to predict the spectral radiative properties of VACNT arrays in the broad infrared spectrum.

The purpose of this paper is to theoretically investigate the radiative properties for VACNT coatings from the near- to far-infrared wavelengths (1 μm to 1000 μm). The optical constants of individual CNTs are modeled based on the available data of graphite, treated with a coordinate transform. The anisotropic dielectric functions of the VACNT array are obtained using an effective medium approximation that treats the VACNT array with a certain volume filling ratio (packing density) as a homogeneous film. Misalignment is also considered using a component weighting method that has been shown to be valid for multiwalled CNT arrays from the visible to mid-infrared [16]. Radiative properties are calculated with both incidence angle and wavelength sweeps to illustrate the conditions needed for effective absorption by the VACNT films.

2 Dielectric Functions

To determine the optical properties of VACNT arrays, the molecular structure of the constituent CNT filaments must be understood. CNTs have been formed by thermal catalytic decomposition of hydrocarbons at metal catalyst particle sites during a plasma-enhanced chemical vapor deposition process [24–26].

[1]Corresponding author.
Manuscript received March 12, 2014; final manuscript received November 12, 2014; published online May 14, 2015. Assoc. Editor: L. Q. Wang.

Multiwalled CNTs were characterized to have graphitic layers formed parallel to the growth direction [27]. For VACNTs, one can visualize them as many graphene sheets rolled together into tubes and positioned on a flat horizontal substrate at one end of the tube. Considering the structure similarity, it is reasonable to model the optical properties of the multiwalled VACNT array based on those of graphite, which is an anisotropic material, as discussed in Sec. 2.1.

2.1 Dielectric Functions Graphite. Graphite is a semimetal and characterized by its layered structure, where each individual layer or sheet is called graphene. The electrical conductivity along the sheet (in the x–y plane) is much higher than that across the layers (in the z direction). Graphite is also an optically anisotropic medium whose optical axis is parallel to the z-axis. The dielectric permittivity is characterized by a diagonal tensor. The in-plane component (ε_{xx} or ε_{yy}) is for the ordinary waves, for which the electric field is perpendicular to the optical axis, and can be denoted by $\varepsilon_{\perp}$. The out-of-plane component (ε_{zz}) is for the extraordinary wave, for which the electric field is parallel to the optical axis, and can be denoted by $\varepsilon_{||}$.

The absorption of carbon-related materials in the visible and UV is due to the electronic transition between the π and π^* bands at the M point of the hexagonal Brillouin zone that has a bandgap in the UV region [28–30]. On the other hand, the far-infrared absorption for ordinary waves in graphite is due to the interband transition and free electrons [31,32]. The interband absorption was first observed by Sato [31] and can be attributed to the interlayer interactions that result in a bandgap of about 0.01–0.02 eV at the H point of the Brillouin zone [30]. A similar bandgap or pseudogap was observed for CNTs in the far-infrared, although with varying strengths and locations, which have been attributed to the curvature and intertube interactions [17,20,22,33]. For extraordinary waves, only weak free-electron absorption exists in graphite that dominates its optical properties at wavelengths longer than 20 μm [34]. Lattice vibrations were also observed with sharp absorption peaks in the mid-infrared for both ordinary and extraordinary waves [35].

Due to the difficulties in preparing highly oriented crystalline graphite, there exist large variations in the experimental spectroscopic data [36,37]. The Kramers–Kronig relations have commonly been used to obtain the dielectric function if the normal reflectance of a material is obtained in a large spectrum and reasonably extrapolated to zero and infinite frequencies [38]. The tabulated optical constants listed in Palik's handbook do not cover wavelengths beyond 62 μm and there are no data between 0.7 μm and 10 μm for the extraordinary component [36]. Philipp [32] performed a comprehensive analysis of the reflectance of graphite for ordinary waves by combining their earlier experimental data from 0.04 eV to 26 eV [39] with those from Sato [31] between 0.006 eV and 0.04 eV. The far-infrared dielectric function was fitted to a Drude free-electron model, allowing the extension to longer wavelengths up to 1240 μm [32,37]. Philipp's work [32] was re-analyzed by Draine and Lee [37] in combination with results published by other groups, added with the lattice vibration band around 1587 cm^{-1} (6.30 μm) using the Lorentz model parameters obtained by Nemanich et al. [35]. Venghaus [34] measured the reflectance of pyrolytic graphite for normal incidence on a cleaved surface with electric field parallel to the optical axis in the wavelength region from 2.5 μm to 100 μm and fitted with a Drude model for the far-infrared. Draine and Lee [37] combined this work with other studies on the extraordinary dielectric function of graphite, including the Lorentz model centered at 868 cm^{-1} (11.5 μm) due to the out-of-plane phonon mode [35].

In the present study, the dielectric functions (excluding the phonon vibration and free-electron contribution) are extracted mainly from the plots of Ref. [37]. Then, the Drude model [32,34] and Lorentz model [35] are superimposed to the extracted dielectric functions. The complex dielectric function is related to the optical constants by $\varepsilon = (n + i\kappa)^2$, where n and κ are the refractive index and extinction coefficient, respectively. The optical constants of graphite thus obtained are shown in Fig. 1 for both ordinary and extraordinary waves in the wavelength region: $1\,\mu\text{m} < \lambda < 1000\,\mu\text{m}$. Both $n_{\perp}$ and $\kappa_{\perp}$ increase with wavelength and clearly show a metallic behavior [40]. Interband transition plays an important role on the optical constants for $30\,\mu\text{m} < \lambda < 100\,\mu\text{m}$ as shown in Fig. 1(*a*). On the contrary, $n_{||}$ is nearly constant and $\kappa_{||} \ll n_{||}$ for $1\,\mu\text{m} < \lambda < 10\,\mu\text{m}$, as shown in Fig. 1(*b*). Hence, graphite behaves as an absorbing dielectric in this wavelength region. Free-electron absorption dominates beyond 20 μm and toward long wavelengths, $n_{||} \approx \kappa_{||}$, and both increase with wavelength according to the Hagen–Rubens relation [40]. In the far-infrared, however, the values of $n_{||}$ and $\kappa_{||}$ are much smaller than their counterparts $n_{\perp}$ and $\kappa_{\perp}$. Lattice vibrations give rise to sharp peaks at $\lambda = 6.3$ μm and 11.5 μm in the ordinary and extraordinary components, respectively. These peaks may not necessarily be observed for CNTs [16,17].

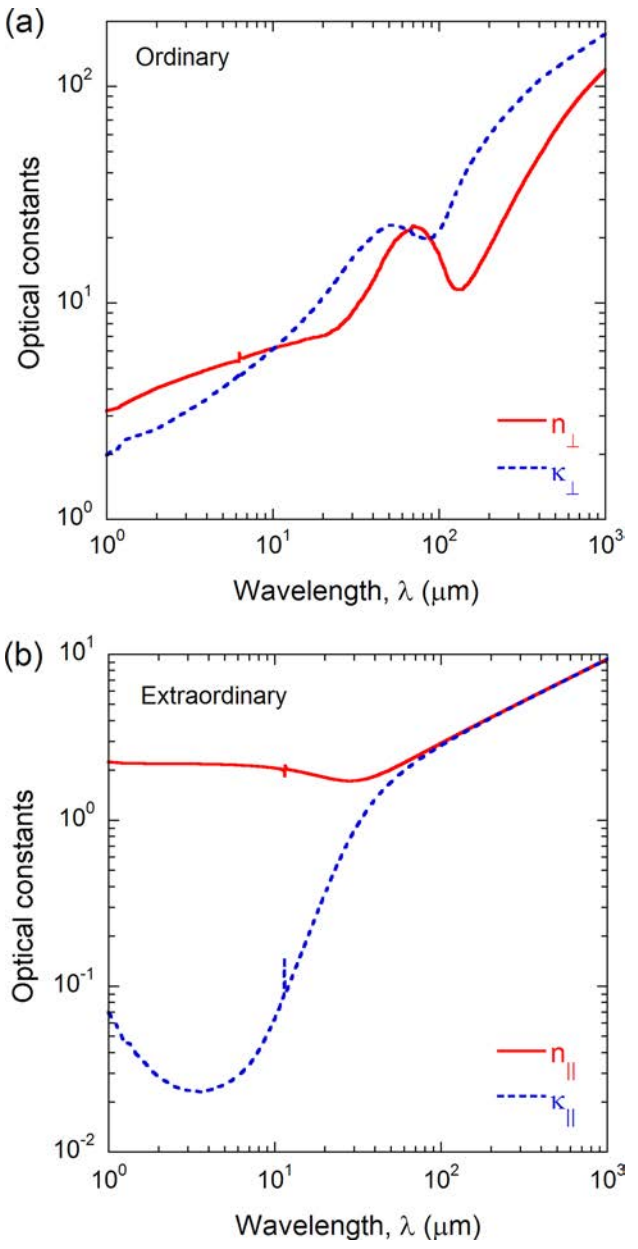

Fig. 1 Optical constants (n and κ) of graphite: (*a*) electric field perpendicular to the optical axis and (*b*) electric field parallel to the optical axis

2.2 Effective Medium Approximation for VACNT Films. Figure 2(*a*) shows a representative array of VACNTs on a silicon substrate. The inset shows a square unit cell viewed from above with a CNT of diameter d and width a, assuming that the CNTs form an aligned periodic array. Perfectly aligned CNTs versus imperfectly aligned CNTs are schematically shown in Figs. 2(*b*) and 2(*c*), respectively.

The VACNT coating or film is an inhomogeneous medium since it is composed of periodic CNTs and voids (either air or vacuum). The effective medium theory (EMT) can be applied to homogenize the medium [41–43], provided that the wavelength of the incident electromagnetic radiation is much longer than the period a, which typically ranges from 50 nm to 150 nm, based on the 10–30 nm diameter of CNTs [1,44]. These dimensions are much smaller than the shortest wavelength of interest of 1000 nm. Although EMT does not consider the local diffraction and antenna effects that are accounted for in finite-difference time-domain analysis [45], it is a reasonably fast and simple method that is well-suited for modeling the far-field optical properties of CNTs especially in the infrared spectrum [46].

In essence, VACNT arrays can be treated as a uniaxial medium whose optical axis is parallel to the tube or along the z-axis. Based on the Maxwell–Garnett theory and coordinate transform, the effective dielectric functions for perfectly aligned CNT films can be expressed in terms of the filling ratio and the dielectric functions of graphite as [15,41]

$$\varepsilon_{\text{eff,O}} = \frac{\varepsilon_{||}(1+f) + \sqrt{\varepsilon_{||}/\varepsilon_{\perp}}(1-f)}{\varepsilon_{||}(1-f) + \sqrt{\varepsilon_{||}/\varepsilon_{\perp}}(1+f)} \tag{1}$$

$$\varepsilon_{\text{eff,E}} = f\varepsilon_{\perp} + (1-f) \tag{2}$$

where f is the volume filling ratio that can be estimated by $\pi d^2/4a^2$ using notation from Fig. 2(*a*). The subscripts O and E signify ordinary and extraordinary components, respectively.

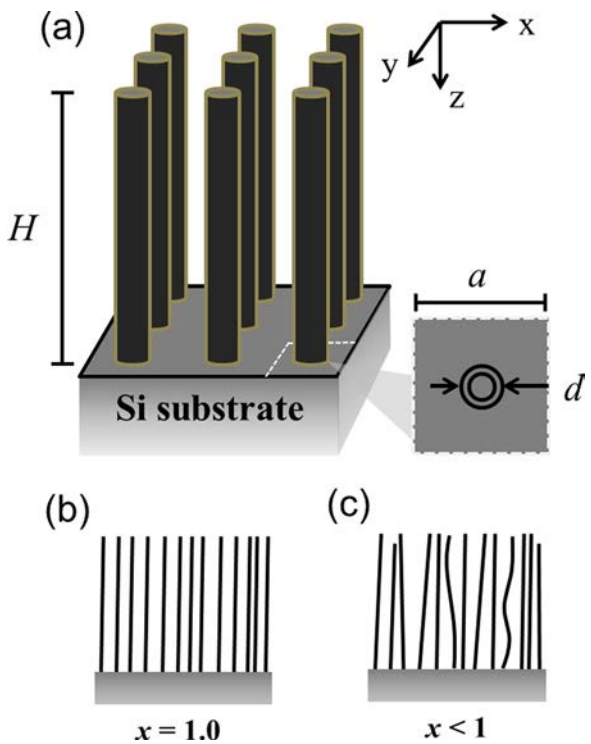

Fig. 2 (*a*) Illustration of a VACNT film of thickness *H* grown on a silicon substrate, where the inset shows a unit cell of width *a* containing a multiwalled CNT of diameter *d* for a periodic array; (*b*) perfectly aligned CNTs with an alignment factor $x = 1.0$; and (*c*) imperfectly aligned CNTs where $x < 1$. Typical VACNT coatings have alignment factor ranging from $x = 0.95$ to $x = 0.99$.

Considering defects from sample fabrication such as random tilting and entanglements, the dielectric functions are modified with a weighting constant x called degree of alignment or alignment factor. The alignment factor for a perfectly aligned albeit experimentally unfeasible VACNT array is $x = 1$, as illustrated in Fig. 2(*b*). The misalignment is quantified with $x < 1$ as shown in Fig. 2(*c*). For typical CVD-grown VACNT samples, x ranges between 0.950 and 0.995 [16]. The dielectric functions, obtained from spectroscopy fitting of fabricated VACNT films with varying concentrations of defects, are calculated from the following [15,16]:

$$\varepsilon_{\text{O}} = x\varepsilon_{\text{eff,O}} + (1-x)\varepsilon_{\text{eff,E}} \tag{3}$$

and

$$\varepsilon_{\text{E}} = x\varepsilon_{\text{eff,E}} + (1-x)\varepsilon_{\text{eff,O}} \tag{4}$$

The dielectric function of CNT films approximated by EMT is therefore dependent on both filling ratio and alignment factor. It should be noted that the component weighted model is only applied for slight misalignment, when x is sufficiently large. Furthermore, for perfectly aligned case when $x = 1$, the extinction coefficient for ordinary waves will be extremely small, resulting in an unrealistically large penetration depth at near normal incidence. Using this dielectric function model, the present authors have recently shown that CNT films can greatly enhance near-field radiative heat transfer [46].

The predicted optical constants of VACNT films are plotted in Fig. 3 for wavelengths from 1 μm to 1000 μm. A filling ratio ($f = 0.05$) and alignment factor ($x = 0.98$), obtained experimentally by Ye et al. [16], are taken as the base case. Both parameters are slightly varied individually to illustrate the effect of these deviations on the CNT optical constants. The range of filling ratio in fabricated VACNT films is typically from 0.01 to 0.15 [15]. At wavelengths from 1 μm to about 30 μm, n_{O} is close to 1 and κ_{O} is relatively small; this results in an impedance matching and high absorptance for incidence from air at least for normal incidence. In this region, n_{O} is insensitive to both f and x, κ_{O} depends on both because decreasing the packing density or alignment factor can result in less loss (or a reduction of κ_{O}). Beyond 30 μm, the effect of interband transition results in a resonance feature that appears in the optical constants of VACNT. Furthermore, free-electron absorption becomes important beyond 100 μm, resulting in an increase in the predicted optical constants of CNTs toward longer wavelengths. While the trends of extraordinary optical constants are similar, the values are much higher than the corresponding ordinary optical constants, especially κ_{E}, which is about an order of magnitude higher than κ_{O}. At longer wavelengths, the filling ratio affects the optical constants significantly. On the other hand, only the ordinary components appear to be dependent on the alignment factor. This is because the extraordinary optical constants are much greater than the ordinary counterparts; subsequently, a small change in alignment factor has a bigger impact on the weighted average according to Eq. (3).

The dielectric function model presented in Eqs. (1) and (2) is in good agreement with the mid-infrared transmittance measurements at normal incidence [16]. The optical constants obtained in the far-infrared, especially for the extraordinary components, are much higher than those reported in Ref. [23], by transmission ellipsometry in the wavelengths between 750 μm and 190 μm. The disagreement could be due to the CNT density or filament structure of the fabricated VACNT samples. It should also be mentioned that while interband transitions were also observed for single-walled CNTs, the strength is often much weaker than that in graphite [17]. Because of the limited data on the far-infrared optical properties of CNTs, the optical constants of graphite are adopted in the present work.

3 Radiative Properties of VACNT Films

The radiative properties of a semi-infinite uniaxial medium can be formulated using the surface admittance or impedance [47].

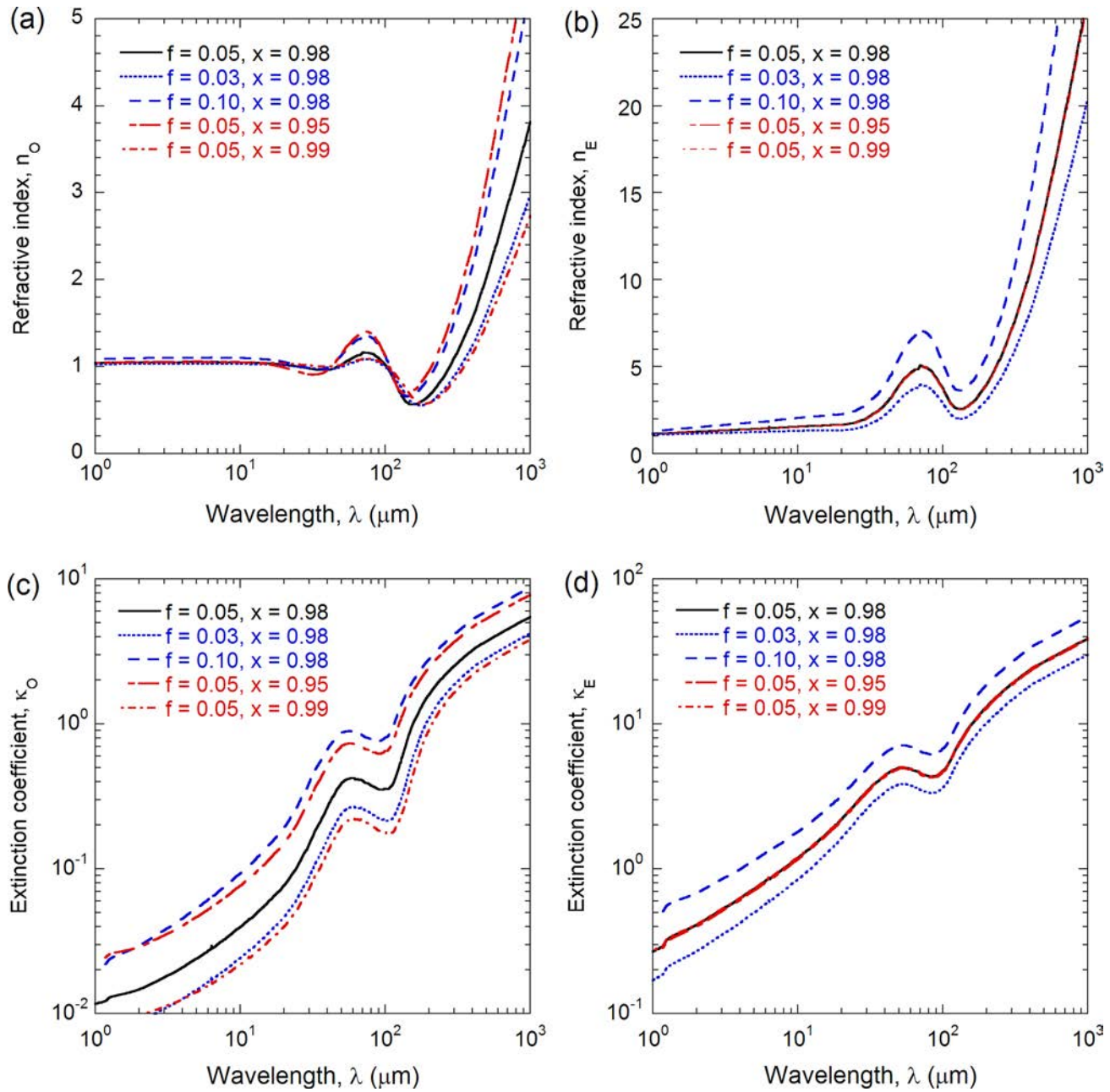

Fig. 3 Effective optical constants of VACNT films with varying filling ratios *f* and alignment factors *x*: (*a*) and (*b*) refractive index for ordinary and extraordinary waves, respectively and (*c*) and (*d*) extinction coefficient for ordinary and extraordinary waves, respectively

Detailed formulation including the thin film case can be found from previous publications [48,49]. For VACNT, however, since the optical axis is perpendicular to the interface, the method for calculating the radiative properties for isotropic medium [40] can be used with a modification to the perpendicular wave vector component. Note that for a plane wave incident at an angle θ_i in the x–z plane, the wavevector components in air (medium 1) are $k_x = k_0 \sin\theta_i$ and $k_{z,1} = k_0 \cos\theta_i$, where $k_0 = 2\pi/\lambda$. Note that k_x is the same in all layers. For transverse electric wave or s-polarization, the VACNT behaves like an isotropic medium with the ordinary wave optical constants. The z-component wavevector in the VACNT layer (medium 2) for s-polarization is therefore

$$k_{z,2} = \frac{2\pi}{\lambda}\sqrt{\varepsilon_O - \sin^2\theta_i} \tag{5}$$

For transverse magnetic wave or p-polarization, we have [49]

$$k_{z,2} = \frac{2\pi}{\lambda}\sqrt{\varepsilon_O - \frac{\varepsilon_O}{\varepsilon_E}\sin^2\theta_i} \tag{6}$$

The Fresnel reflectance and transmittance for extraordinary waves (p-polarization) between air and VACNT can be expressed as

$$r_{12,p} = \frac{k_{z,1} - k_{z,2}/\varepsilon_O}{k_{z,1} + k_{z,2}/\varepsilon_O} \tag{7}$$

and

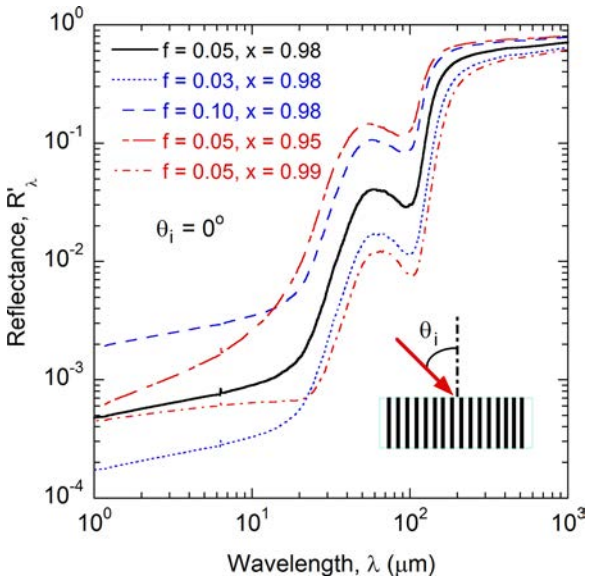

Fig. 4 Normal reflectance spectra of a semi-infinite VACNT films with varying filling ratios and alignment factors. The incidence angle upon the VACNT film is illustrated in the inset.

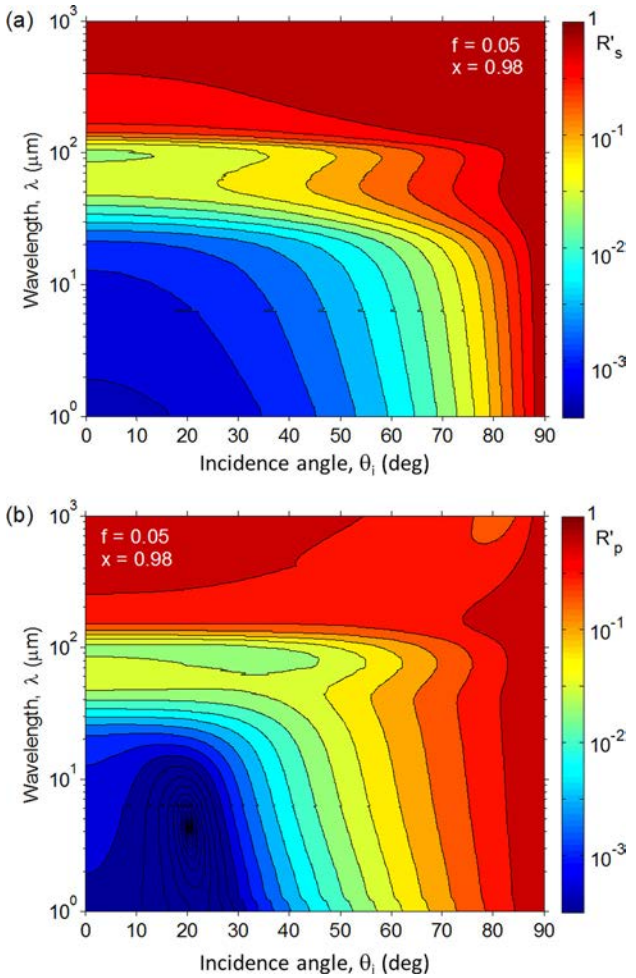

Fig. 5 Contours of the reflectance versus wavelength and incidence angle for: (*a*) s-polarization and (*b*) p-polarization. The VACNT film is assumed to be semi-infinite with filling ratio $f = 0.05$ and alignment factor $x = 0.98$.

$$t_{12,p} = \frac{2k_{z,1}}{k_{z,1} + k_{z,2}/\varepsilon_O} \tag{8}$$

The reflectance of a semi-infinite VACNT medium is calculated by $R'_\lambda = |r_{12}|^2$ for each polarization. Furthermore, Airy's formulae can be applied to obtain the reflectance and transmittance for a CNT film on a substrate [40].

3.1 Reflectance of Semi-Infinite CNT Films. The normal reflectance of a VACNT medium is shown in Fig. 4 for varying filling ratios and alignment factors. At $\lambda < 20$ μm, the reflectance $R'_\lambda < 0.01$ for all cases and $R'_\lambda < 0.0015$ in the case for $f = 0.05$ and $x = 0.98$ (default). Reducing the filling ratio can further reduce the reflectance. In the interband transition region ($30\ \mu\text{m} < \lambda < 100\ \mu\text{m}$), the reflectance increases to 0.03–0.04 in the default case and differs greatly with the changes in either f or x.

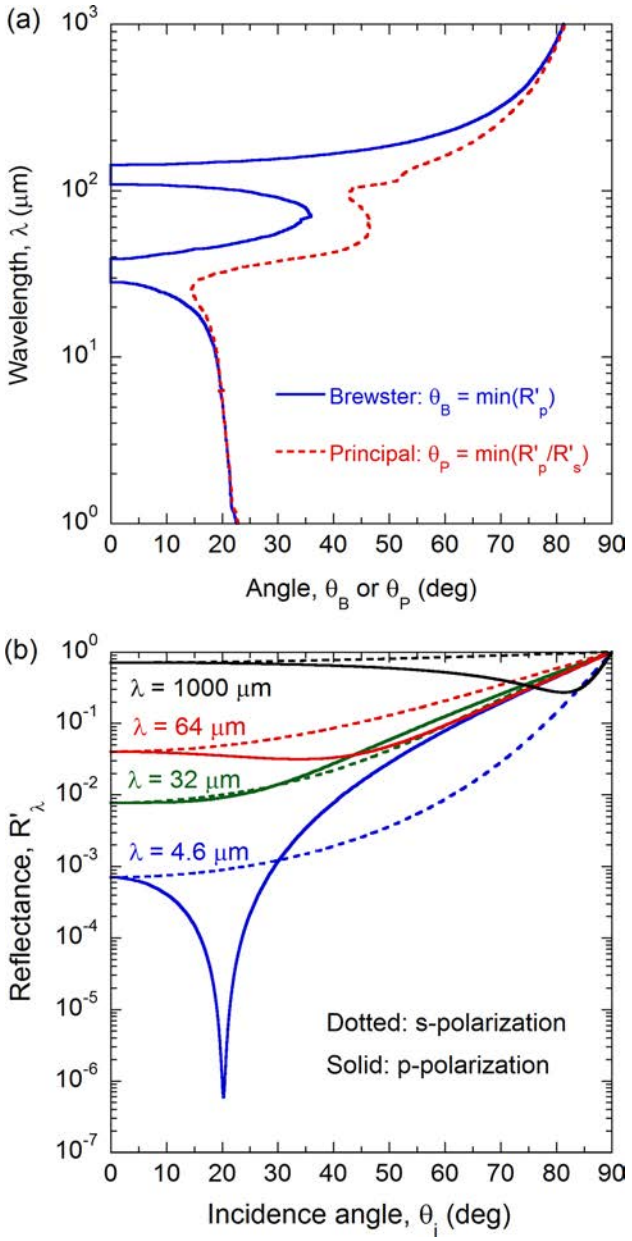

Fig. 6 (*a*) Correlation of the Brewster angle θ_B and the principal angle θ_P with the wavelength. The abscissa and ordinate are interchanged in order to compare the traces with Fig. 5(*b*). (*b*) The reflectance as a function of the incidence angle for both polarizations at four distinct wavelengths.

VACNT becomes highly reflecting at far-infrared ($R'_\lambda > 0.5$) when the wavelength exceeds 200 μm for the default case and the reflectance is smaller with reduced filling ratio or increased alignment factor. It appears that the filling ratio affects more in the near- to mid-infrared region, while the alignment factor has a stronger effect in the far-infrared. The absorptance, $\alpha'_\lambda = 1 - R'_\lambda$, is very close to unity in the near- and mid-infrared region. In the far-infrared, the absorptance decreases; however, reducing the filling ratio and improving alignment can increase the absorptance. It should be noted that high absorptance was reported for single-walled VACNT films at wavelengths up to 200 μm [13]. The observed high absorptance may be due to the reduction of the interband and free-electron absorption, along with surface roughness effects that could enhance radiation absorption.

To study the angular and polarization dependence, the contour plots of reflectance for s- and p-polarization are shown in Fig. 5 for $f = 0.05$ and $x = 0.98$. The contour traces identify the isoreflectance lines. For s-polarization, the reflectance increases with the angle of incidence for all wavelengths, as shown in Fig. 5(*a*). Furthermore, the reflectance increases with wavelength similar to the case for normal incidence. At the grazing angle, $\theta_i = 90$ deg, the reflectance for both polarizations approaches unity as expected. However, for p-polarizations, the reflectance may reach a minimum at an oblique angle. As shown in Fig. 5(*b*), there is a global minimum at $\lambda = 4.6$ μm and $\theta_i = 20.2$ deg, where reflectance sharply drops by several orders of magnitude. This phenomenon is further explored in Sec. 3.2.

3.2 Brewster Angle and Principal Angle. The incidence angle at which the reflectance becomes zero for p-polarization is defined as the Brewster angle θ_B, at which all the incident energy is transmitted into the medium [40,50]. Perfect transmission holds for a lossless dielectric medium only. For real materials, the angle at which R'_p is minimized is called the Brewster angle, which may not exist for a high loss medium. Materials with well-defined Brewster angles are frequently used as angular polarizers. The wavelength-dependent Brewster angles of VACNT coatings are shown in Fig. 6(*a*). The abscissa and ordinate are interchanged so that one can refer the location of the Brewster angle with the minimum of R'_p in Fig. 5(*b*). Note the Brewster angle is not defined for 28 μm $< \lambda <$ 39 μm and for 110 μm $< \lambda <$ 142 μm. The principal angle θ_P is defined as the minimum of the ratio of the p-polarized to the s-polarized reflectance [50]. The principal angle is also shown in Fig. 6(*a*) and can be defined for all wavelengths. At wavelengths $\lambda < 10$ μm where loss is small, the Brewster angle and principal angle are close to each other. For an isotropic dielectric medium with $n > 1$, the Brewster angle is always greater than 45 deg. This does not hold in general for an anisotropic medium [14].

The angular behavior is further explored by calculating the angular-dependent reflectance for each polarization at different wavelengths, as shown in Fig. 6(*b*). At $\lambda = 4.6$ μm, the p-polarization reflectance drops sharply at the Brewster angle ($\theta_B = 20.2$ deg), by several orders of magnitude. At this wavelength, the Brewster angle and principal angle are coincident. In the case of $\lambda = 32$ μm, the Brewster angle is undefined and R'_p increases monotonically with θ_i. For $\lambda = 64$ μm, R'_p exhibits a shallow dip around 34 deg, and there is a large mismatch between θ_B and θ_P. At $\lambda = 1000$ μm, where $\theta_B \approx \theta_P$, there is a distinct dip in R'_p at 81.3 deg. Therefore, the mismatch between the Brewster angle and principal angle in Fig. 6(*a*) indicates the wavelength region where the Brewster angle becomes poorly defined.

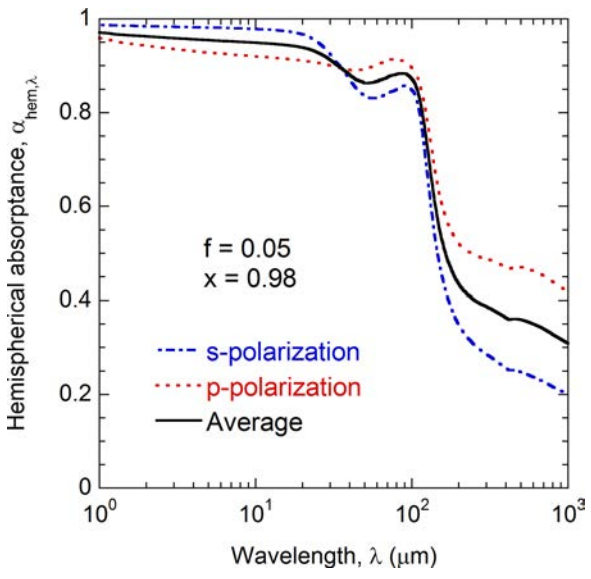

Fig. 7 Hemispherical absorptance spectra for s- and p-polarization, and the average of the two

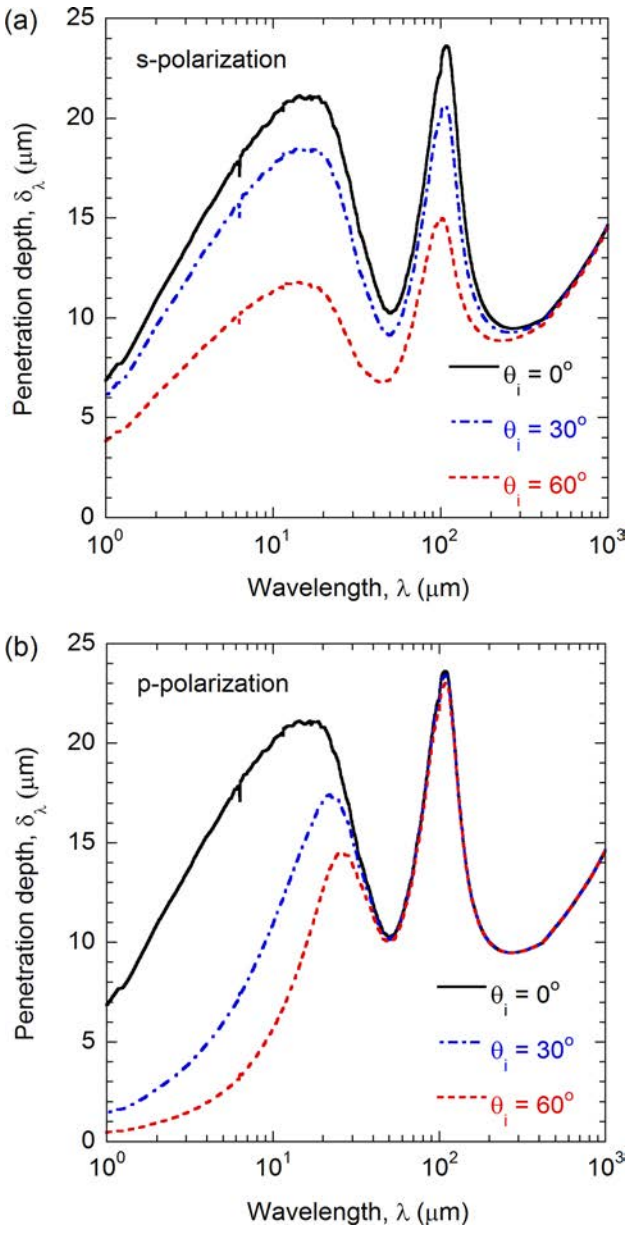

Fig. 8 Radiation penetration depths for: (*a*) s-polarization and (*b*) p-polarization at incidence angles $\theta_i = 0$ deg, 30 deg, and 60 deg, with $f = 0.05$ and $x = 0.98$

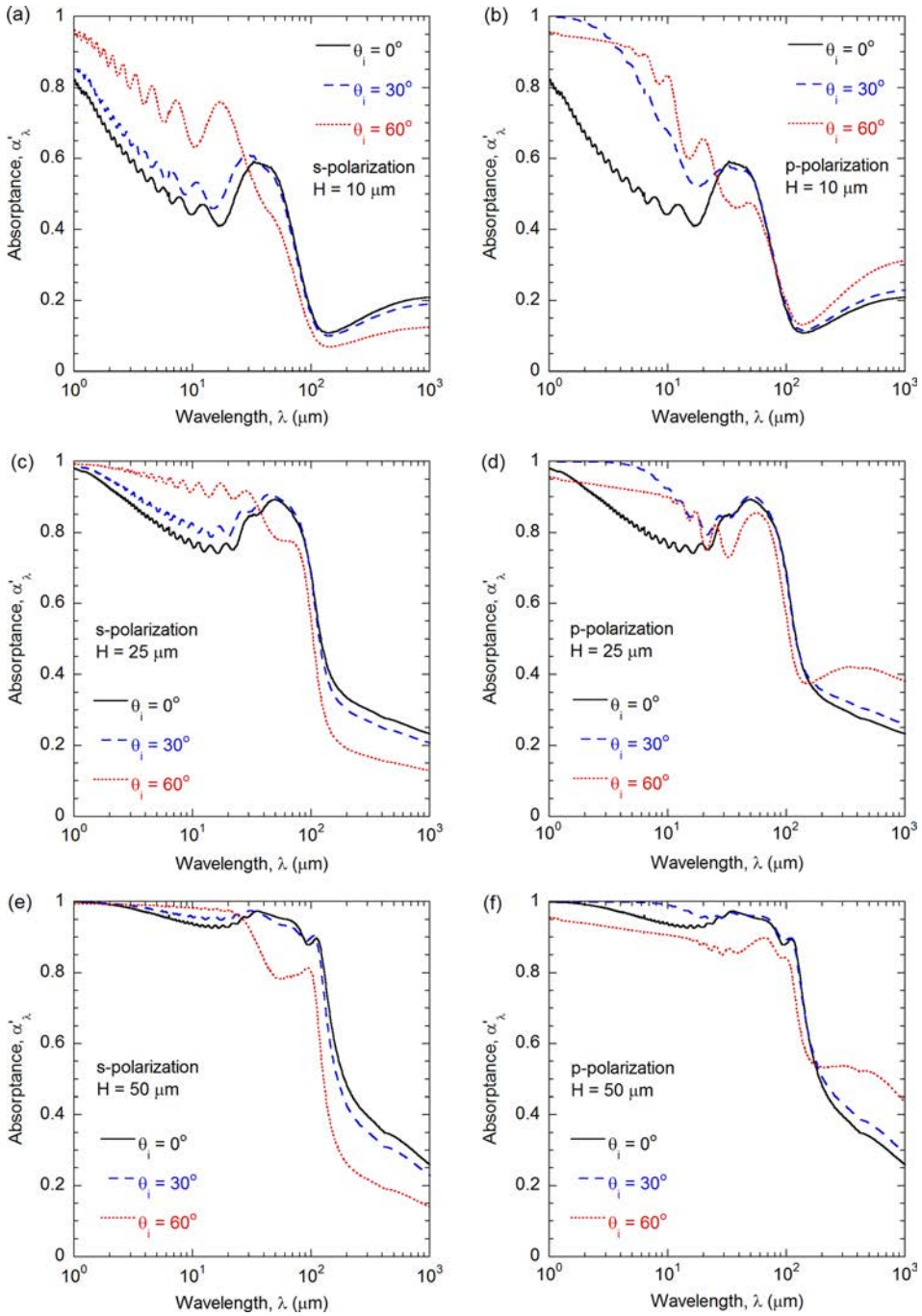

Fig. 9 Absorptance of VACNT film of different thicknesses with $f = 0.05$ and $x = 0.98$, at incidence angles of $\theta_i = 0$ deg, 30 deg, and 60 deg: (*a*) s-polarization, $H = 10$ μm; (*b*) p-polarization, $H = 10$ μm; (*c*) s-polarization, $H = 25$ μm; (*d*) p-polarization, $H = 25$ μm; (*e*) s-polarization, $H = 50$ μm; and (*f*) p-polarization, $H = 50$ μm

3.3 Hemispherical Absorptance. The directional-spectral emittance is integrated over the solid angle ($d\Omega = \cos\theta_i \sin\theta_i \, d\theta_i d\phi_i$) to obtain the hemispherical emittance $\varepsilon_{\text{hem},\lambda}$ [40]

$$\varepsilon_{\text{hem},\lambda} = \frac{1}{\pi}\int_0^{2\pi}\int_0^{\pi/2} \varepsilon'_\lambda \cos\theta_i \sin\theta_i d\theta_i d\phi_i \tag{9}$$

According to Kirchhoff's law, the directional-spectral absorptance is equal to the directional-spectral emittance ε'_λ, if the temperature of the material is uniform at least within several penetration depths [40]. This states that $\varepsilon'_\lambda = \alpha'_\lambda = 1 - R'_\lambda$ for a semi-infinite medium. If the intensity of the incident radiation is independent of the direction (diffuse incidence), then the hemispherical absorptance equals the hemispherical emittance: $\alpha_{\text{hem},\lambda} = \varepsilon_{\text{hem},\lambda}$.

The hemispherical absorptance spectra are shown in Fig. 7, for both s- and p-polarizations, as well as their average, for the default f and x values. In the near- and mid-infrared region, the hemispherically integrated absorptance is higher (exceeding 0.98 at $\lambda < 15$ μm) for s-polarized incident waves. At wavelengths longer than 40 μm, the hemispherical absorptance for p-polarization is higher than that for s-polarization. In general, the hemispherical absorptance is smaller than the normal absorptance due to angular dependence, although surface roughness can give rise to increased hemispherical absorptance [12].

3.4 Penetration Depth. It is important to examine the penetration depth in order to determine how thick the VACNT film is needed for it to be opaque so that the substrate effect is negligible. The radiation penetration depth is defined as where the power of the electromagnetic wave entering the medium will decay by $e^{-1} \approx 37\%$ from the interface. The spectral penetration depth can be expressed as [40]

$$\delta_\lambda = \frac{1}{2\mathrm{Im}(k_{z,2})} \tag{10}$$

where $k_{z,2}$ is the z-component wavevector given in Eqs. (5) and (6) for s- and p-polarizations, respectively. The predicted penetration depths for both polarizations are shown in Fig. 8 from the near- to far-infrared. At normal incidence, the penetration depth becomes $\delta_\lambda = \lambda/(4\pi\kappa_O)$ regardless of the polarization status, where κ_O is plotted in Fig. 3(*c*). In the near-infrared, penetration depth increases up to $\delta_\lambda = 21\ \mu$m around $\lambda = 15\ \mu$m. Because of the interband transition, the penetration depth decreases to about $\delta_\lambda = 10\ \mu$m around $\lambda = 50\ \mu$m. The penetration depth then increases to reach a peak at wavelength slightly longer than 100 μm, which is beyond the interband transition and before the Drude model takes effect in the far-infrared. Here, the penetration depth reaches up to $\delta_\lambda = 23.6\ \mu$m. There is another minimum in δ_λ at wavelengths between 200 μm and 300 μm. As the wavelength further increases, δ_λ increases with the square root of wavelength, as predicted by the Drude free-electron model [40].

The angular dependence of the penetration depth is different for s- and p-polarizations. This can be understood by the different expressions in Eqs. (5) and (6). In the near-infrared, the penetration depth decreases with increasing incidence angle in a similar way for both polarizations since the ordinary and extraordinary dielectric functions are of the same order of magnitude close to unity. At very long wavelengths beyond 500 μm, the term with $\sin^2\theta_i$ in Eqs. (5) and (6) has little effect and therefore, the penetration depth is independent of the angle of incidence. In the intermediate region, because the magnitude of ε_O is smaller than that of ε_E, the penetration depth for p-polarization becomes independent of θ_i at a relatively shorter wavelength of about 50 μm. Based on the penetration depth, CNTs with a thickness greater than 100 μm can generally be considered opaque, because the height or thickness H of the CNT film is greater than four times the maximum penetration depth. Thinner film coatings are often desired to reduce material consumption and growth time. The effect of thickness and substrate on the absorptance of CNT films is discussed next.

3.5 Thin Film Effects. The absorptance spectra of VACNT of different thickness on Si substrate are shown in Fig. 9 for both polarizations at different angles of incidence and with varying CNT film thicknesses. The absorptance is calculated by $\alpha'_\lambda = 1 - R'_\lambda - T'_\lambda$, so that only the absorptance by the CNT film is included. In the calculation, the optical constants of lightly doped Si are taken from Ref. [51] and extended to the far-infrared by assuming a constant refractive index of 3.42 and negligible loss. At normal incidence, the results for both polarizations are the same.

For the 10 μm-thick VACNT thin film, as shown in Figs. 9(*a*) and 9(*b*), the absorptance is significantly reduced. For normal incidence, the maximum absorptance is $\alpha'_\lambda = 0.8$ at $\lambda = 1\ \mu$m and decreases with wavelength until $\lambda = 20\ \mu$m. Interference effects can be clearly observed in the near- and mid-infrared region. The interband transition causes an absorptance peak at wavelengths between 50 μm and 100 μm. At $\lambda = 100\ \mu$m, corresponding to the maximum penetration depth peaks, the CNT absorption is minimum at $\alpha'_\lambda = 0.1$. At short wavelengths, increasing the angle of incidence gives rise to a higher absorptance due to the decreasing penetration depth as shown in Fig. 8. However, for p-polarization, the absorptance is higher at $\theta_i = 30$ deg than 60 deg due to the Brewster angle at which the reflection coefficient at the air–CNT interface is minimized around 20 deg. The outcome is complicated due to the interplay of interference, internal absorption, and surface reflection. Interestingly, at longer wavelengths ($\lambda > 100\ \mu$m), the absorptance improves toward oblique incidence for p-polarization, but reduces for s-polarization. This can be explained by interface reflection being higher for s-polarization than that for p-polarization as illustrated in Figs. 5 and 6(*b*). Furthermore, the Brewster angle is relatively large and the reflection coefficients decrease with increasing θ_i for p-polarization. This trend is the same for all three CNT thicknesses because it is related to the interface effect rather than internal absorption.

Increasing the thickness of the VACNT film improves absorptance (especially in the near- and mid-infrared) and reduces interference effects. This can be seen by comparing the trends from figures for each polarization in Fig. 9 from top to bottom. The interference effect almost diminishes for $H = 50\ \mu$m, as shown from Figs. 9(*e*) and 9(*f*) and the absorptance is closer to that of semi-infinite medium except for regions with large penetration depths. Calculations were also made for $H = 100\ \mu$m with slight differences from those for $H = 50\ \mu$m; this suggests that for most wavelength regions, a CNT thickness of $H = 50\ \mu$m can be approximated as semi-infinite.

4 Conclusions

The radiative properties of multiwalled VACNT coatings are investigated by assuming that the nanotubes exhibit similar dielectric properties as that of coordinate-transformed graphite. Due to the refractive index matching in the near- to mid-infrared, surface reflection is low and the material becomes a good absorber. Due to the interband transition at $\lambda \approx 100\ \mu$m and free-electron effect in the far-infrared, the reflectance is high, resulting in a rather low absorption at $\lambda > 100\ \mu$m. Generally, low packing density and high degree of alignment can reduce surface reflection. Also, the Brewster angle is best defined only in the near- and far-infrared, as matching with the principal angle is qualified. For thin CNT films, absorptance in the near- and mid-infrared is deteriorated due to high penetration depth and reflection at the CNT–substrate interface. It is thus recommended to grow the coating of thickness greater than 50 μm to preserve the characteristic high absorptance of VACNT. The method present here and the detailed results may assist in the design of VACNT coatings for broadband infrared applications.

Acknowledgment

This work was supported by the National Science Foundation under CBET-1235975 (for RZZ and ZMZ) and the Department of Energy, Office of Science, Basic Energy Sciences under DE-FG02-06ER46343 (for XLL and ZMZ).

Nomenclature

a = CNT unit cell period (m)
d = carbon nanotube diameter (m)
f = filling ratio (i.e., packing density)
H = CNT coating thickness (m)
k = wavevector (m^{-1})
n = refractive index
r = Fresnel reflection coefficient
R' = directional reflectance
t = Fresnel transmission coefficient
T' = directional transmittance
x = alignment factor

Greek Symbols

α_{hem} = hemispherical absorptance
α' = directional absorptance
δ = penetration depth (m)
ε = dielectric function
$\varepsilon_{\mathrm{hem}}$ = hemispherical emittance
ε' = directional emittance

θ = polar angle (deg)
κ = extinction coefficient
λ = wavelength in vacuum (m)
ϕ = azimuthal angle (deg)
Ω = solid angle (sr)

Subscripts

B = Brewster angle
eff = effective medium
E or O = extraordinary or ordinary waves
i = incident
m,n = index
p or s = p- or s-polarization
P = principal angle
1 or 2 = medium 1 or 2
λ = spectral
$\parallel$ = parallel (extraordinary)
$\perp$ = perpendicular (ordinary)

References

[1] Zhang, Z. M., and Ye, H., 2013, "Measurement of Radiative Properties of Engineered Micro-Nanostructures," Annu. Rev. Heat Transfer, **16**(16), pp. 345–396.
[2] Tarasov, M., Svensson, J., Kuzmin, L., and Campbell, E. E. B., 2007, "Carbon Nanotube Bolometers," Appl. Phys. Lett., **90**(16), p. 163503.
[3] Itkis, M. E., Borondics, F., Yu, A., and Haddon, R. C., 2006, "Bolometric Infrared Photoresponse of Suspended Single-Walled Carbon Nanotube Films," Science, **312**(5772), pp. 413–416.
[4] Lehman, J., Sanders, A., Hanssen, L., Wilthan, B., Zeng, J., and Jensen, C., 2010, "Very Black Infrared Detector From Vertically Aligned Carbon Nanotubes and Electric-Field Poling of Lithium Tantalate," Nano Lett., **10**(9), pp. 3261–3266.
[5] Lehman, J. H., Hurst, K. E., Radojevic, A. M., Dillon, A. C., and Osgood, R. M., Jr., 2007, "Multiwall Carbon Nanotube Absorber on a Thin-Film Lithium Niobate Pyroelectric Detector," Opt. Lett., **32**(7), pp. 772–774.
[6] Lehman, J. H., Engtrakul, C., Gennett, T., and Dillon, A. C., 2005, "Single-Wall Carbon Nanotube Coating on a Pyroelectric Detector," Appl. Opt., **44**(4), pp. 483–488.
[7] Theocharous, E., Deshpande, R., Dillon, A. C., and Lehman, J., 2006, "Evaluation of a Pyroelectric Detector With a Carbon Multiwalled Nanotube Black Coating in the Infrared," Appl. Opt., **45**(6), pp. 1093–1097.
[8] Chen, C., Lu, Y., Kong, E. S., Zhang, Y., and Lee, S.-T., 2008, "Nanowelded Carbon-Nanotube-Based Solar Microcells," Small, **4**(9), pp. 1313–1318.
[9] Lenert, A., Bierman, D. M., Nam, Y., Chan, W. R., Celanovic, I., Soljacic, M., and Wang, E. N., 2014, "A Nanophotonic Solar Thermophotovoltaic Device," Nat. Nanotechnol., **9**(2), pp. 126–130.
[10] de Heer, W. A., Bacsa, W. S., Châtelain, A., Gerfin, T., Humphrey-Baker, R., Forro, L., and Ugarte, D., 1995, "Aligned Carbon Nanotube Films: Production and Optical and Electronic Properties," Science, **268**(5212), pp. 845–847.
[11] Yang, Z.-P., Ci, L., Bur, J. A., Lin, S.-Y., and Ajayan, P. M., 2008, "Experimental Observation of an Extremely Dark Material Made by a Low-Density Nanotube Array," Nano Lett., **8**(2), pp. 446–451.
[12] Yang, Z.-P., Hsieh, M.-L., Bur, J. A., Ci, L., Hanssen, L. M., Wilthan, B., Ajayan, P. M., and Lin, S.-Y., 2011, "Experimental Observation of Extremely Weak Optical Scattering From an Interlocking Carbon Nanotube Array," Appl. Opt., **50**(13), pp. 1850–1855.
[13] Mizuno, K., Ishii, J., Kishida, H., Hayamizu, Y., Yasuda, S., Futaba, D. N., Yumura, M., and Hata, K., 2009, "A Black Body Absorber From Vertically Aligned Single-Walled Carbon Nanotubes," Proc. Nat. Acad. Sci. USA, **106**(15), pp. 6044–6047.
[14] Wang, X. J., Wang, L. P., Adewuyi, O. S., Cola, B. A., and Zhang, Z. M., 2010, "Highly Specular Carbon Nanotube Absorbers," Appl. Phys. Lett., **97**(16), p. 163116.
[15] Wang, X. J., Flicker, J. D., Lee, B. J., Ready, W. J., and Zhang, Z. M., 2009, "Visible and Near-Infrared Radiative Properties of Vertically Aligned Multi-Walled Carbon Nanotubes," Nanotechnology, **20**(21), p. 215704.
[16] Ye, H., Wang, X. J., Lin, W., Wong, C. P., and Zhang, Z. M., 2012, "Infrared Absorption Coefficients of Vertically Aligned Carbon Nanotube Films," Appl. Phys. Lett., **101**(14), p. 141909.
[17] Ugawa, A., Rinzler, A. G., and Tanner, D. B., 1999, "Far-Infrared Gaps in Single-Wall Carbon Nanotubes," Phys. Rev. B, **60**(16), p. R11305.
[18] Maine, S., Koechlin, C., Rennesson, S., Jaeck, J., Salort, S., Chassagne, B., Pardo, F., Pelouard, J.-L., and Haïdar, R., 2012, "Complex Optical Index of Single Wall Carbon Nanotube Films From the Near-Infrared to the Terahertz Spectral Range," Appl. Opt., **51**(15), pp. 3031–3035.
[19] Kampfrath, T., von Volkmann, K., Aguirre, C. M., Desjardins, P., Martel, R., Krenz, M., Frischkorn, C., Wolf, M., and Perfetti, L., 2008, "Mechanism of the Far-Infrared Absorption of Carbon-Nanotube Films," Phys. Rev. Lett., **101**(26), p. 267403.
[20] Nishimura, H., Minami, N., and Shimano, R., 2007, "Dielectric Properties of Single-Walled Carbon Nanotubes in the Terahertz Frequency Range," Appl. Phys. Lett., **91**(1), p. 011108.
[21] Maeng, I., Kang, C., Oh, S. J., Son, J.-H., An, K. H., and Lee, Y. H., 2007, "Terahertz Electrical and Optical Characteristics of Double-Walled Carbon Nanotubes and Their Comparison With Single-Walled Carbon Nanotubes," Appl. Phys. Lett., **90**(5), p. 051914.
[22] Kumar, S., Kamaraju, N., Moravsky, A., Loutfy, R. O., Tondusson, M., Freysz, E., and Sood, A. K., 2010, "Terahertz Time Domain Spectroscopy to Detect Low-Frequency Vibrations of Double-Walled Carbon Nanotubes," Eur. J. Inorg. Chem., **2010**(27), pp. 4363–4366.
[23] Paul, M. J., Kuhta, N. A., Tomaino, J. L., Jameson, A. D., Maizy, L. P., Sharf, T., Rupesinghe, N. L., Teo, K. B. K., Inampudi, S., Podolskiy, V. A., Minot, E. D., and Lee, Y.-S., 2012, "Terahertz Transmission Ellipsometry of Vertically Aligned Multi-Walled Carbon Nanotubes," Appl. Phys. Lett., **101**(11), p. 111107.
[24] Puretzky, A. A., Geohegan, D. B., Jesse, S., Ivanov, I. N., and Eres, G., 2005, "In situ Measurements and Modeling of Carbon Nanotube Array Growth Kinetics During Chemical Vapor Deposition," Appl. Phys. A, **81**(2), pp. 223–240.
[25] Murakami, Y., Chiashi, S., Miyauchi, Y., Hu, M., Ogura, M., Okubo, T., and Maruyama, S., 2004, "Growth of Vertically Aligned Single-Walled Carbon Nanotube Films on Quartz Substrates and Their Optical Anisotropy," Chem. Phys. Lett., **385**(3–4), pp. 298–303.
[26] Kim, D.-H., Jang, H.-S., Kim, C.-D., Cho, D.-S., Yang, H.-S., Kang, H.-D., Min, B.-K., and Lee, H.-R., 2003, "Dynamic Growth Rate Behavior of a Carbon Nanotube Forest Characterized by In Situ Optical Growth Monitoring," Nano Lett., **3**(6), pp. 863–865.
[27] Baker, R. T. K., 1989, "Catalytic Growth of Carbon Filaments," Carbon, **27**(3), pp. 315–323.
[28] Saito, R., Grüneis, A., Samsonidze, G. G., Dresselhaus, G., Dresselhaus, M. S., Jorio, A., Cançado, L. G., Pimenta, M. A., and Souza Filho, A. G., 2004, "Optical Absorption of Graphite and Single-Wall Carbon Nanotubes," Appl. Phys. A, **78**(8), pp. 1099–1105.
[29] Jäger, C., Henning, T., Schlögl, R., and Spillecke, O., 1999, "Spectral Properties of Carbon Black," J. Non-Cryst. Solids, **258**(1–3), pp. 161–179.
[30] Kuzmenko, A. B., van Heumen, E., Carbone, F., and van der Marel, D., 2008, "Universal Optical Conductance of Graphite," Phys. Rev. Lett., **100**(11), p. 117401.
[31] Sato, Y., 1968, "Optical Study of Electronic Structure of Graphite," J. Phys. Soc. Jpn., **24**(3), pp. 489–492.
[32] Philipp, H. R., 1977, "Infrared Optical Properties of Graphite," Phys. Rev. B, **16**(6), pp. 2896–2900.
[33] Itkis, M. E., Niyogi, S., Meng, M. E., Hamon, M. A., Hu, H., and Haddon, R. C., 2002, "Spectroscopic Study of the Fermi Level Electronic Structure of Single-Walled Carbon Nanotubes," Nano Lett., **2**(2), pp. 155–159.
[34] Venghaus, H., 1977, "Infrared Reflectance and Dielectric Properties of Pyrolytic Graphite for E ‖ c Polarization," Phys. Status Solidi B, **81**(1), pp. 221–225.
[35] Nemanich, R. J., Lucovsky, G., and Solin, S. A., 1977, "Infrared Active Optical Vibrations of Graphite," Solid State Commun., **23**(2), pp. 117–120.
[36] Borghesi, A., and Guizzetti, G., 1991, "Graphite (C)," *Handbook of Optical Constants of Solids II*, E. D. Palik, ed., Academic Press, San Diego, CA, pp. 449–460.
[37] Draine, B. T., and Lee, H. M., 1984, "Optical-Properties of Interstellar Graphite and Silicate Grains," Astrophys. J., **285**(1), pp. 89–108.
[38] Smith, D. Y., 1985, "Dispersion Theory, Sum Rules, and Their Application to the Analysis of Optical Data," *Handbook of Optical Constants of Solids*, E. D. Palik, ed., Academic Press, San Diego, CA, pp. 35–68.
[39] Taft, E. A., and Philipp, H. R., 1965, "Optical Properties of Graphite," Phys. Rev., **138**(1A), pp. A197–A202.
[40] Zhang, Z. M., 2007, *Nano/Microscale Heat Transfer*, McGraw-Hill, New York.
[41] García-Vidal, F. J., Pitarke, J. M., and Pendry, J. B., 1997, "Effective Medium Theory of the Optical Properties of Aligned Carbon Nanotubes," Phys. Rev. Lett., **78**(22), pp. 4289–4292.
[42] Lü, W., Dong, J., and Li, Z.-Y., 2000, "Optical Properties of Aligned Carbon Nanotube Systems Studied by the Effective-Medium Approximation Method," Phys. Rev. B, **63**(3), p. 033401.
[43] Wu, X. H., Pan, L. S., Fan, X. J., Xu, D., Hua, L., and Zhang, C. X., 2003, "A Semi-Analytic Method for Studying Optical Properties of Aligned Carbon Nanotubes," Nanotechnology, **14**(11), pp. 1180–1186.
[44] de los Arcos, T., Garnier, M. G., Oelhafen, P., Seo, J. W., Domingo, C., García-Ramos, J. V., and Sánchez-Cortés, S., 2005, "In Situ Assessment of Carbon Nanotube Diameter Distribution With Photoelectron Spectroscopy," Phys. Rev. B, **71**(20), p. 205416.
[45] Bao, H., Ruan, X., and Fisher, T. S., 2010, "Optical Properties of Ordered Vertical Arrays of Multi-Walled Carbon Nanotubes From FDTD Simulations," Opt. Express, **18**(6), pp. 6347–6359.
[46] Liu, X. L., Zhang, R. Z., and Zhang, Z. M., 2013, "Near-Field Thermal Radiation Between Hyperbolic Metamaterials: Graphite and Carbon Nanotubes," Appl. Phys. Lett., **103**(21), p. 213102.
[47] Knoesen, A., Moharam, M., and Gaylord, T., 1985, "Electromagnetic Propagation at Interfaces and in Waveguides in Uniaxial Crystals," Appl. Phys. B, **38**(3), pp. 171–178.
[48] Wang, H., Liu, X., Wang, L., and Zhang, Z., 2013, "Anisotropic Optical Properties of Silicon Nanowire Arrays Based on the Effective Medium Approximation," Int. J. Therm. Sci., **65**, pp. 62–69.
[49] Liu, X. L., Wang, L. P., and Zhang, Z. M., 2013, "Wideband Tunable Omnidirectional Infrared Absorbers Based on Doped-Silicon Nanowire Arrays," ASME J. Heat Transfer, **135**(6), p. 061602.
[50] Born, M., and Wolf, E., 1999, *Principles or Optics*, 7th ed., Cambridge University Press, Cambridge, UK.
[51] Edwards, D. F., 1985, "Silicon (Si)," *Handbook of Optical Constants of Solids*, E. D. Palik, ed., Academic Press, San Diego, pp. 547–569.